Journal of Oceanology and Limnology
Vol. 44, No. 2, pp. 603-615, 2026
https://doi.org/10.1007/s00343-025-5112-2

Research Paper

Geochemical signatures of hydrothermal sediments on the ultraslow-spreading Gakkel Ridge, Arctic Ocean*

Wensheng XUE, Yejian WANG**, Zhongyan QIU, Chi YANG, Chunguo YANG, Xinyu MA, Tao ZHANG

State Key Laboratory of Submarine Geoscience, Second Institute of Oceanography, Ministry of Natural Resources, Hangzhou 310012, China

Received Apr. 8, 2025; accepted in principle May 28, 2025; accepted for publication Jun. 16, 2025

Abstract More than 721 submarine hydrothermal fields have been documented globally, however, the characterization of hydrothermal systems beneath the ice-covered Arctic Ocean remains poorly constrained. During the 2021 JASMInE expedition, a 369-cm-long sediment core was recovered from the central rift valley of the Gakkel Ridge 96°E. The core is predominantly composed of terrigenous debris, Fe-(oxyhydr)oxides, volcanic glass, and hydrogenetic Mn oxides. Three hydrothermal-affected layers (HA1–HA3) within the upper 85 centimeters below seafloor (cmbsf) exhibit enrichment in Fe, Cu, Pb, P, V, Mg, Ca, and Na, associated with accumulation of Fe-(oxyhydr)oxides and volcanic glass. Among these, Layer HA2 (13–16 centimeters below seafloor (cmbsf)) displays the most intense hydrothermal signature, characterized by high concentrations of Fe (12.06–15.22 wt.%), Mn (2 687–5 465 μg/g), Cu (245–373 μg/g), and Pb (248–342 μg/g), accompanied by reduced rare earth element (REE) concentrations, and shale-normalized patterns featuring negative Ce anomalies, and positive Eu anomalies. In comparison, Layers HA1 (83–85 cmbsf) and HA3 (6–7 cmbsf) exhibit only marginally elevated concentrations of hydrothermal-related elements (Fe, Cu, Pb, P, V) compared to pelagic background sediments, indicating a weaker hydrothermal influence. Overall, the observed coarsening of volcanic glass grain size and its increased abundance within hydrothermal-affected layers, coupled with diagnostic signatures from the Al-Fe-Mg ternary diagram and the detection of hydrothermal plume anomalies along the 100° E Axial Volcanic Ridge (AVR), collectively point to a basalt-hosted hydrothermal system associated with the AVR as the source of the hydrothermal signals recorded in the core. These findings reveal the geochemical fingerprints of hydrothermal materials in Arctic deep-sea sediments, offering new insights into their sources and formation processes in the ice-covered ocean.

Keyword: ice-covered ocean; hydrothermal event; sediment core; major and trace element; Gakkel Ridge

1 INTRODUCTION

Mid-ocean ridge hydrothermal systems constitute pivotal contributors to global marine geochemical cycles, delivering substantial fluxes of dissolved elements and particulate matter into oceanic water columns while influencing sediment composition across basin scales (German and Seyfried, 2014; Früh-Green et al., 2022). Hydrothermal sediments have emerged as critical archives for reconstructing the evolution of seafloor hydrothermal activities due to their enrichment in diagnostic metallic elements and mineral assemblages (Mills et al., 1993; Evans et al., 2023; Pelleter et al., 2024). These sediments not only preserve physicochemical information of vent fluids, but their geochemical characteristics can also reveal elemental transport and enrichment patterns during hydrothermal plume dispersal (Coogan et al., 2017; Liao et al., 2018; Wang et al., 2024). Such insights are essential for understanding

* Supported by the National Key Research and Development Program of China (No. 2021YFF0501304), the National Natural Science Foundation of China (No. 41976076), and the United Nations Decade of Ocean Science for Sustainable Development Project: Arctic Deep Observation for Multi-sphere Cycling (ADOMIC) (No. 2021-2030)

** Corresponding author: yjwang@sio.org.cn

the geochemical behaviors of submarine hydrothermal systems (Agarwal et al., 2020; Yang et al., 2022). As polygenetic mixtures, hydrothermal sediments incorporate non-hydrothermal components such as biogenic detritus, pelagic clays, authigenic minerals, and volcanic glass (Cave et al., 2002; Liao et al., 2018). The occurrence states and phase evolution characteristics of these constituents provide critical insights into identifying hydrothermal material transport pathways and their environmental response mechanisms (März et al., 2010; Gartman et al., 2024).

The ultraslow-spreading Gakkel Ridge in the Arctic Ocean is currently the least studied mid-ocean ridge in terms of hydrothermal activity research (Edmond et al., 2003; Albers et al., 2025). Initial investigations during the 2001 AMORE expedition identified extensive hydrothermal plumes along the ridge axis (6°W–85°E), with physicochemical anomalies suggesting venting from ≥9 discrete sites predominantly associated with axial volcanic edifices (Edmond et al., 2003; Michael et al., 2003). Subsequent observations from the 2007 AGAVE cruise confirmed hydrothermal signals at the 85°E axial volcanic ridge and its northern rift wall (Stranne et al., 2010). To date, only two active vent fields, which named the Aurora Field and Polaris Field have been documented along the Gakkel Ridge 6°W–85°E, both of them are considered be co-controlled by both mafic crust and deeper ultramafic sources (German et al., 2016, 2022; Albers et al., 2025).

In contrast, seafloor hydrothermal activities along the volcanically sparse eastern segment of the Gakkel Ridge 85°E remain understudied. Previous studies identified two disperse axial volcanic ridges within the 92°E–100°E segment (Ding et al., 2022), reflecting the focused magma eruption processes on the spreading axis (Zhang et al., 2024). This tectonic background suggests significant magma activities differences in geological settings between the eastern and western segment of the Gakkel Ridge (Cochran, 2008), potentially influencing seafloor hydrothermal circulation. Hence, this study integrates sedimentological, mineralogical, and geochemical analyses of a sediment core from Gakkel Ridge 96°E to identify hydrothermal activity signals and discuss the main factors influencing the type variations of hydrothermal systems along the entire Gakkel Ridge.

2 GEOLOGICAL SETTING

The Gakkel Ridge, located in the Eurasian Basin of the eastern Arctic Ocean, is encircled by continents and shelves. As the deepest and slowest-spreading mid-ocean ridge globally, it exhibits a progressive decrease in full spreading rates from 1.4 cm/a adjacent to the Lena Trough to 0.6 cm/a approaching the Siberian continental margin (Michael et al., 2003; Cochran, 2008; German et al., 2022). Distinct from most mid-ocean ridges, this system lacks transform faults but maintains a continuous rift valley morphology (O'Connor et al., 2021). This study focuses on the eastern segment of Gakkel Ridge spanning from 92°E to 100°E longitude, which features two axial volcanic ridges (AVRs) at its terminal boundaries (Fig.1). Geophysical data reveal significant crustal thickening beneath these volcanic edifices, with maximum thicknesses of 8.0 and 8.9 km beneath the western (92°E) and eastern (100°E) AVRs, respectively. In contrast, the adjacent rift zones display thinner crust (3–4 km), highlighting spatial heterogeneity in crustal architecture (Zhang et al., 2024). These structural variations suggest focused melt accretion beneath the AVRs (Tan et al., 2024; Zhang et al., 2024). Additionally, sedimentary accumulations exceeding several hundred meters have been identified within the rift zone (Zhang et al., 2024), suggesting limited crustal accretion activity in this region.

3 SAMPLE AND METHOD

A 369-cm gravity core (N12-GR-GC02, hereafter GC02) was recovered from the axial valley floor of the Gakkel Ridge (95.935°E, 85.091°N; water depth: 4 475 m) during the 2021 JASMInE expedition. The sampling site was located between the axial volcanic ridges (AVRs) at 92°E and 100°E, approximately 40 km from both volcanic centers (Fig.1).

All laboratory analyses were conducted at the State Key Laboratory of Submarine Geoscience (SGL), Second Institute of Oceanography (MNR). The core underwent sequential processing: (1) whole-core imaging was performed using a Multi Sensor 604 Core Logger; (2) continuous subsampling was carried out at 1-cm intervals (yielding 369 subsamples); and (3) grain size separation via wet sieving to retain the >63-μm fraction. Microtextural and mineralogical analyses were performed using a Leica stereomicroscope and Zeiss Ultra 55 field-emission scanning electron microscopy (SEM) equipped with an Oxford-Inca X-Max 20 energy-dispersive spectroscopy (EDS) system (operated at 15 kV).

Forty-eight subsamples were freeze-dried at

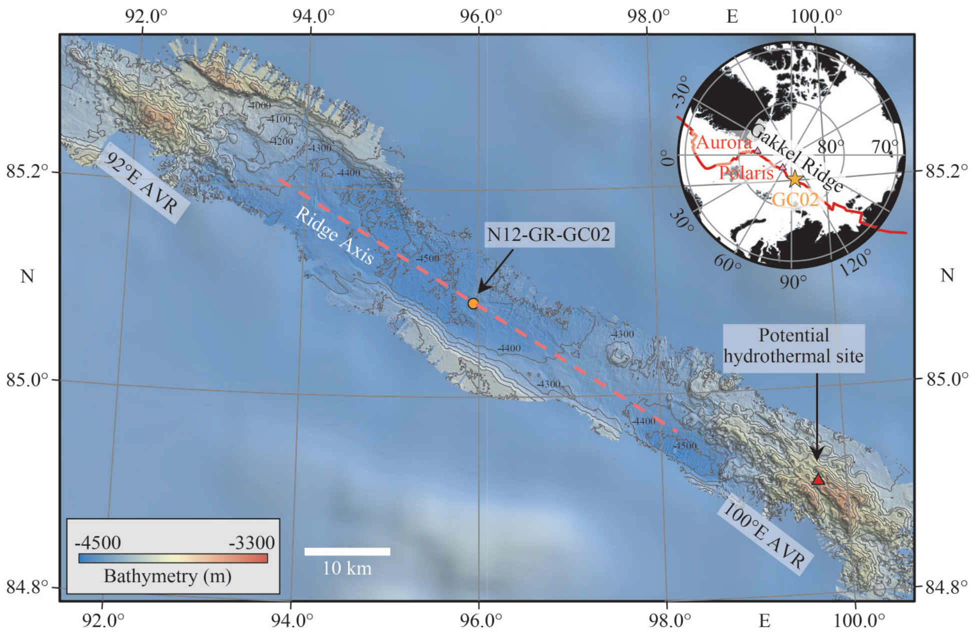

Fig.1 Bathymetric map of the Gakkel Ridge 92°E–100°E segment showing Core GC02 location and volcanic edifices

High-resolution bathymetry data for the axial zone are adapted from Ding et al. (2022), with surrounding areas based on the International Bathymetric Chart of the Arctic Ocean (IBCAO v4.2). Hydrothermal plumes at both 92°E and 100°E AVRs were investigated during the JASMInE expedition, conclusive anomalies were solely observed at the 100°E site (see Supplementary Fig. S1), located ~40 km east of GC02 hole. Projection: WGS 1984 Stereographic North Pole. AVR: axial volcanic ridge.

-50 °C for 72 h using a freeze dryer. The dried samples were ground into fine powders (<75 μm; equivalent to 200 mesh). Bulk mineralogical compositions were determined by X-ray diffraction (XRD) on a PANalytical X'Pert Pro diffractometer equipped with a Cu Kα radiation source, operated at 45 kV and 40 mA. Scans were performed over 3°–70° 2θ range in continuous mode with a step size of 0.016 7° and a scan speed of 0.05 s/step.

Seventy subsamples representing key stratigraphic intervals were pulverized to a fine powder (<200 mesh) using an agate pestle and mortar to ensure homogeneity. For whole-rock major element analysis, loss on ignition (LOI) was first determined by combusting 0.5–1.0 g of powder at 1 000 °C for 90 min, followed by cooling in a desiccator. Subsequently, 0.600 0 g (±0.3 mg) of dried powder was mixed with 6.000 0 g (±0.3 mg) of lithium tetraborate/metaborate flux ($Li_2B_4O_7$:$LiBO_2$:LiBr= 49.75:49.75:0.5) in platinum crucibles, fused at 1 100 °C in an automated furnace (with periodic swirling to eliminate bubbles), and cooled to form homogeneous glass disks. Major element concentrations were quantified using a PANalytical Axios MAX wavelength-dispersive XRF spectrometer. Trace element analysis employed a Thermo iCAP RQ ICP-MS: 50 mg of sample powder was sealed in Teflon bombs with 2.5-mL HF and 0.6-mL HNO_3, heated at 190 °C for 48 h, and repeatedly evaporated to incipient dryness. After re-dissolving and further processing (including a final 190 °C heating for 12 h), solutions were diluted to 100 g with Milli-Q water, spiked with internal standards (Rh+Re, 100 ng/mL each), and stored in 100-mL polyethylene bottles. Analytical accuracy was verified using certified reference materials (JMS-2, AGV-2, BHVO-2). Method precision was ±5% for major oxides (SiO_2, Al_2O_3, Fe_2O_3, MgO, MnO, CaO, Na_2O), ±7% for P_2O_5 and TiO_2, and better than ±10% for trace elements.

Principal component analysis (PCA) was employed to identify sedimentary components in Core GC02. The raw major and trace element data were preprocessed using centered log-ratio (clr) transformation for standardization (Egozcue et al., 2003). Principal components were extracted via correlation matrices in IBM SPSS Statistics 29.0, with orthogonal rotation of the factor loading matrix performed by the Varimax method to reduce variables to linearly independent principal components. The number of principal components was determined based on the Kaiser-Guttman criterion (eigenvalues λ>1) combined with inflection point identification in scree plots. Data suitability for PCA was verified through the Kaiser-Meyer-Olkin (KMO) measure of sampling adequacy and Bartlett's test of sphericity. Elemental associations were interpreted using factor loadings and correlation matrices.

4 RESULT

4.1 Lithology

The Core GC02 preserves a continuous sedimentary sequence with no discernible stratigraphic hiatuses (Fig.2). Particle size analysis (sieving through a 63-μm mesh) revealed virtually no sand-sized or coarser particles, indicating the dominance of fine-grained sediments (silt and clay) throughout the core. The sedimentary succession was classified into three lithological categories based on sediment color, mineralogical assemblages, and bulk geochemical signatures. (1) Pelagic layers. The layers constitute the predominant facies (the constituting intervals were not classified as hydrothermal-affected or manganese-rich layers), and are characterized by yellowish-brown to greyish-green pelagic clays and contains elevated concentrations of quartz, albite, muscovite, illite, chlorite, and so on (Supplementary Fig.S2). A distinctive grey-green clay horizon (121–369 cmbsf) in the lower section exhibits enhanced clay mineral (illite and chlorite etc.) concentrations (Supplementary Fig.S2). (2) Hydrothermal-affected layers (HA1–HA3). These discrete layers occur at 6–7 cmbsf (HA3), 13–16 cmbsf (HA2), and 82–85 cmbsf (HA1) (Fig.2). Layer HA2 exhibits a homogenous reddish-brown coloration, whereas Layers HA1 and HA3 consist predominantly of yellowish-brown to light grey sediments, with intermittent thin reddish-brown laminae. All hydrothermal-affected layers contain coarse-grained (>63 μm) amorphous Fe-(oxyhydr) oxide aggregates (Fig.3a–d), with Layer HA2 displaying the highest concentration of these particles. Volcanic glass fragments are coarser-grained and more abundant in hydrothermal-affected layers compared to adjacent layers (Fig.3a, c–d). XRD analyses reveal that the mineral composition of Layers HA1–HA3 is consistent with pelagic sediments, with no detectable concentrations of sulfides or iron oxides. Notably, HA2 exhibits marked reductions in quartz, albite, and clay mineral contents relative to other strata in Core GC02 (Supplementary Fig.S2). (3) Manganese-rich layers, hereafter Mn-rich layers (M1–M5). Five distinct

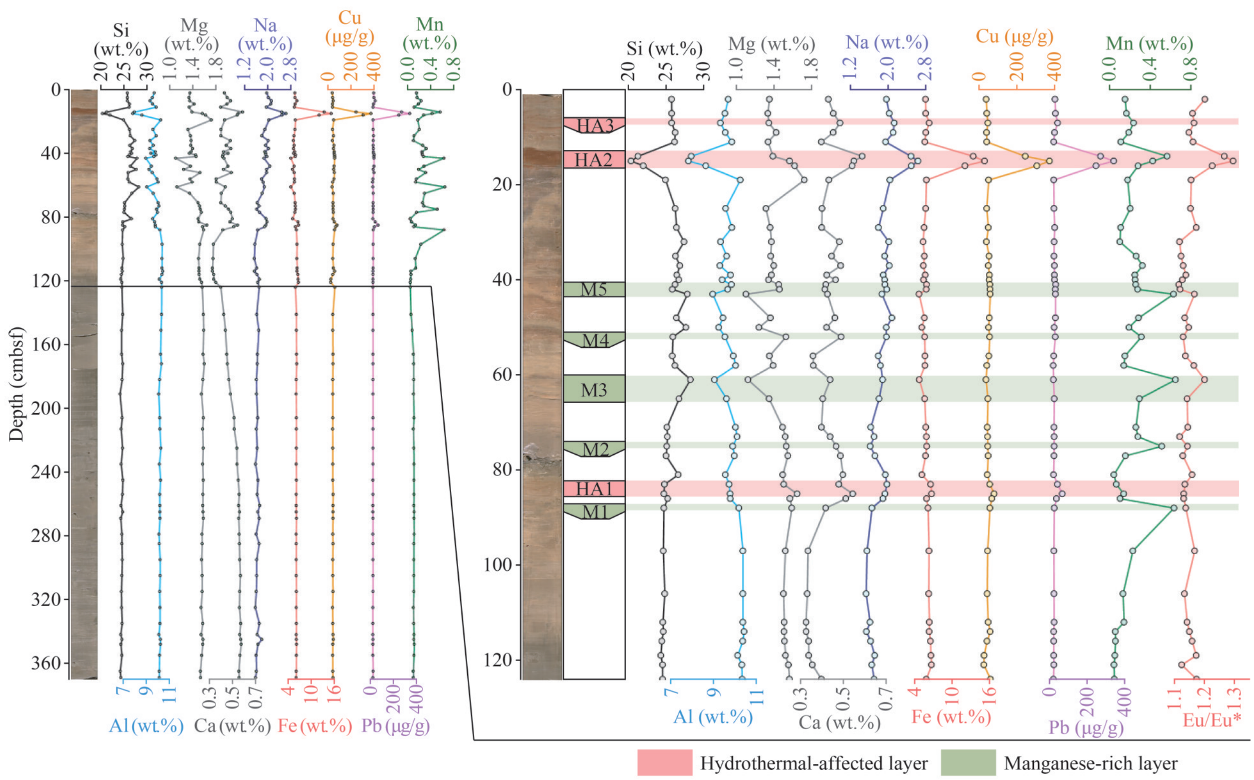

Fig.2 Stratigraphy and downcore distributions of Si, Al, Mg, Ca, Na, Fe, Cu, Pb, Mn, and Eu anomaly (Eu/Eu*) in Core N12-GR-GC02

The core disruption at 78 cmbsf was artificially induced, whereas the core was originally continuous. cmbsf: centimeters below seafloor.

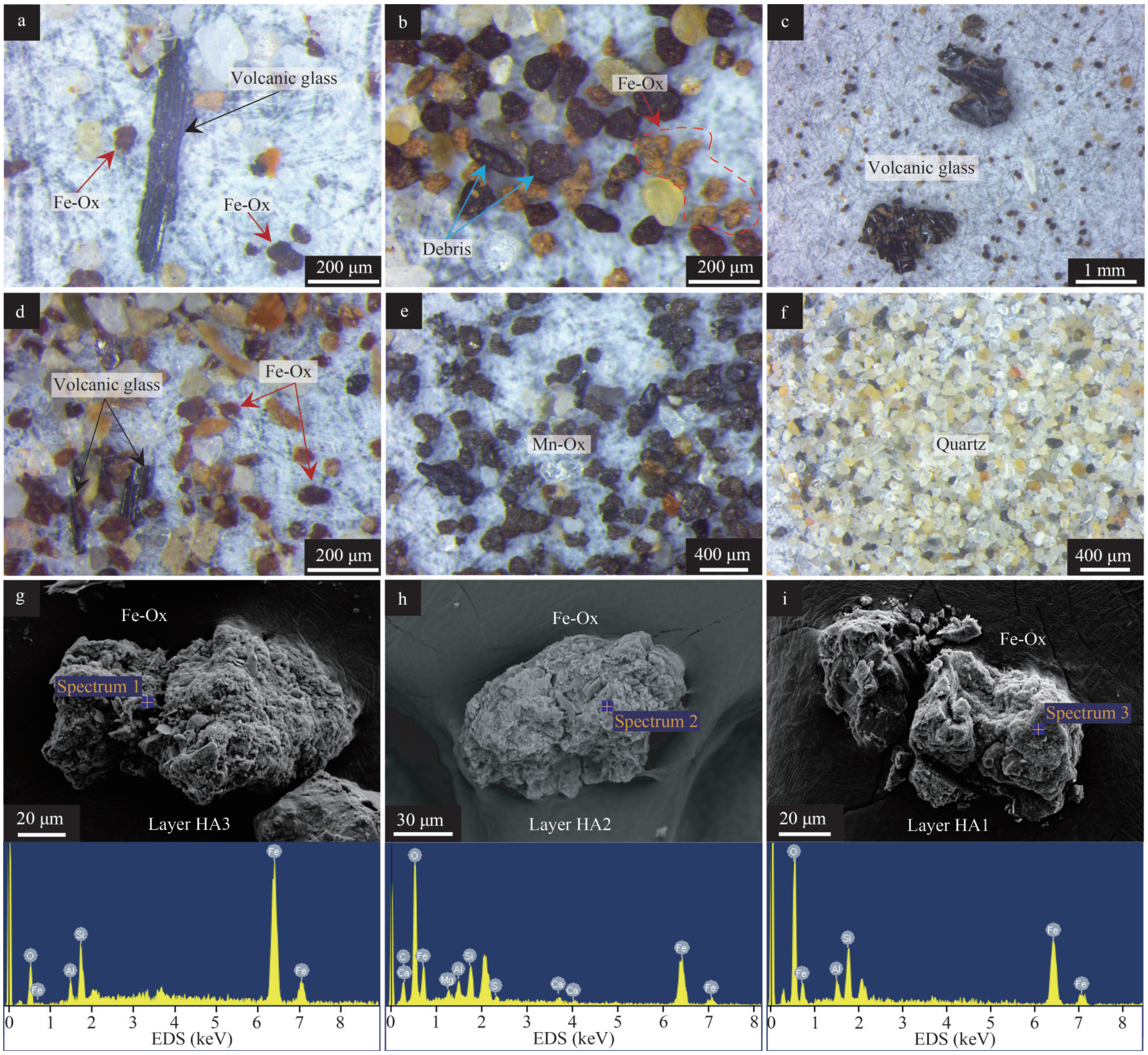

Fig.3 Stereomicroscopic and scanning electron microscope (SEM) images of Core GC02 sediments with corresponding energy-dispersive X-ray spectroscopy (EDS)

a. Fe-(oxyhydr)oxides and coarse volcanic glass in Layer HA3; b. Fe-(oxyhydr)oxides and rock debris (some well-rounded) in Layer HA2; c. coarse volcanic glass (diameter: ~1.5 mm) in Layer HA2; d. Fe-(oxyhydr)oxides and volcanic glass in Layer HA1; e. Mn oxides in Layer M3; f. image of a typical coarse grain from the pelagic layer; g. SEM image and EDS spectrum of Fe-(oxyhydr)oxides in Layer HA3; h. SEM image and EDS spectrum of Fe-(oxyhydr)oxides in Layer HA2; i. SEM image and EDS spectrum of Fe-(oxyhydr)oxides in Layer HA1 (energy in kilo electron volts, keV).

Mn-rich layers were identified at 39–43 cmbsf (M5), 51–52 cmbsf (M4), 61–65 cmbsf (M3), 74–75 cmbsf (M2), and 87–88 cmbsf (M1). These intervals are characterized by the presence of Mn-oxides (Fig.3e), correlating with dark grey patches and bands observed in the core profile (Fig.2). However, X-ray diffraction analysis detected no significant concentrations of Mn oxides, with the mineral assemblage of the Mn-rich layers being consistent with pelagic sediments (Supplementary Fig.S2).

4.2 Geochemistry

4.2.1 Major and trace element compositions

The major and trace elements of Core GC02 are detailed in Supplementary Table S1. The core exhibits a consistently low total calcium content (0.33–0.58 wt.%) and high silicon concentrations (20.34–28.25 wt.%). The low Ca content correlates with the absence of foraminifera as observed under stereomicroscopy, likely resulting from the sampling depth exceeding the carbonate compensation depth

(CCD≈4 000 m; Jutterström and Anderson, 2005). Conversely, the high Si content is attributed to abundant detrital quartz, albite, and clay minerals (Supplementary Fig.S2), as combined stereomicroscopic and SEM observations identified no siliceous bioclasts. Distinct geochemical partitioning occurs across lithological units: pelagic layers exhibit enrichments in Al (9.25–10.43 wt.%) and Ti (0.53–0.60 wt.%), contrasting with a decrease in metal elements including Fe (5.15–6.69 wt.%), Mn (412–3 100 μg/g), Cu (26–60 μg/g), Zn (102–158 μg/g), Pb (20–32 μg/g), Co (16–56 μg/g), and Ni (46–70 μg/g), particularly within the greyish-green clay unit (121–369 cmbsf). Hydrothermal-affected layers (HA1–HA3) exhibit discernible metal enrichment, with Fe (5.90–15.22 wt.%), Mn (713–5 465 μg/g), Cu (47–373 μg/g), Zn (113–166 μg/g), and Pb (37–342 μg/g). Notably, the concentrations of Fe, Cu, Zn, Pb, P, and V in Layer HA2 (mean 13.56 wt.%, 308 μg/g, 155 μg/g, 287 μg/g, 0.37 wt.%, and 763 μg/g, respectively) are about 3.3-, 8.8-, 1.7-, 16.9-, 5.3-, and 5.9-fold higher than those in ridge flank sediments of the Gakkel Ridge (mean 4.14 wt.%, 35 μg/g, 91 μg/g, 17 μg/g, 0.07 wt.%, and 129 μg/g respectively; Rusakov et al., 2010) (Fig.4). Mn-rich horizons (M1–M5) contain elevated Mn (2 539–6 416 μg/g), Co (38–89 μg/g) and Ni (60–83 μg/g) concentrations compared to the pelagic layers.

4.2.2 Rare earth elements and yttrium

Rare earth element (REE) and yttrium (Y) concentrations are presented in Supplementary

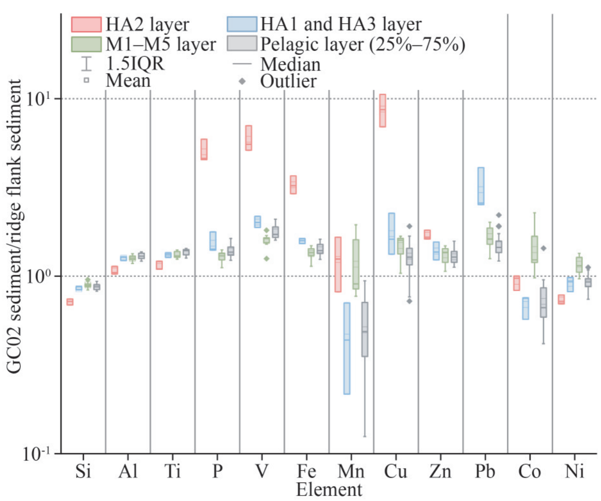

Fig.4 Element composition of sediment from Core GC02

The data of pelagic sediments from the Gakkel Ridge flank (0–94 cmbsf section of Core PS 70/306-3) is sourced from Rusakov et al. (2010). The whiskers of the box plots extend to 1.5 times the interquartile range (IQR).

Table S2. Pelagic layers in Core GC02 exhibit light rare earth elements (LREE) enrichment (La_N/Yb_N= 0.94–1.07), with total REE (ΣREE) concentrations of 188–226 μg/g (mean 201 μg/g; n=55). Layer HA1 displays higher REE concentrations (ΣREE= 222–249 μg/g, mean 236 μg/g; n=2), whereas both Layers HA2 (ΣREE=179–188 μg/g, mean 182 μg/g; n=3) and HA3 (ΣREE=185 μg/g, n=1) show lower values. Overall, the Post-Archean Australian Shale (PAAS; McLennan, 2001) normalized REE patterns of GC02 samples resemble those of sediments from the East Siberian Sea and Laptev Sea (Fig.5). Among these, Laptev Sea sediments exhibit elevated REE contents and a positive Eu anomaly, showing the closest similarity to the samples in this study. Notably, the PAAS normalized rare earth elements and yttrium (REY) patterns reveal a relative depletion in LREE (La_N/Yb_N=0.84–0.88) in Layer HA2, consistent with the hydrothermal sediments from Loki's Castle (Fig.5). This horizon is further characterized by negative Ce anomalies (Ce/Ce*=0.82–0.85) coupled with positive Eu anomalies (Eu/Eu*=1.23–1.30), contrasting with pelagic layers (Ce/Ce*=0.94–1.02; Eu/Eu*=1.12–1.20). Layer HA3 exhibits a marginally negative Ce anomaly (Ce/Ce*=0.96), while Layer HA1 shows neutral to weakly positive Ce anomalies (Ce/Ce*= 0.97–1.05). Mn-rich horizons are distinguished by subtle positive Ce anomalies (Ce/Ce*=1.00–1.05).

5 DISCUSSION

5.1 Provenance discrimination of Core GC02

To differentiate the components of the sediments, the principal component analysis (PCA) was applied to major and trace element concentrations in the 0–121 cmbsf core interval (42 samples), with exclusion of diagenetically altered intervals in 121–369 cmbsf. The analysis yielded three principal component factors (PC1–PC3) with eigenvalues >1, collectively explaining 90.2% of the variance in the dataset (Fig.6). The KMO measure of sampling adequacy was 0.806 (>0.6), while the Bartlett's test of sphericity was significant (P<0.001), confirming suitable variable intercorrelations for multivariate analysis.

PC1 accounted for 51.4% of the variance in the dataset, with high positive loadings (loading≥0.6) including Fe, Cu, Pb, Zn, P, and V, and high negative loadings (loading≤-0.6) for Si (Fig.6). The correlation matrix revealed a statistically significant correlation between Fe, Cu, Pb, P, and V (R=0.85–0.98, n=42, P<0.01). This geochemical assemblage (Fe-

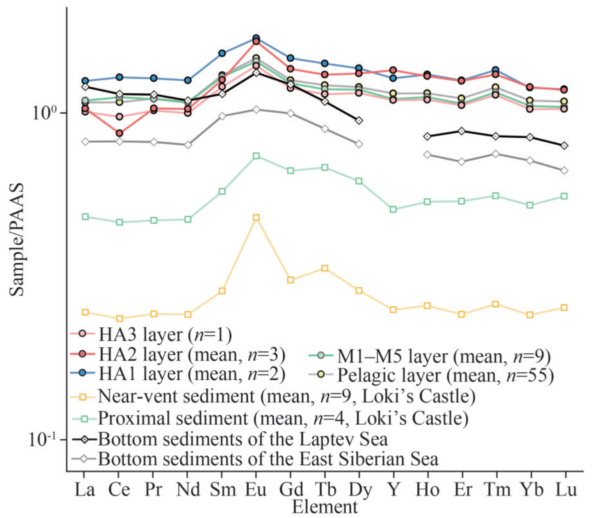

Fig.5 Rare earth element (REE) and yttrium (Y) patterns of bulk sediments of Core GC02, normalized to the Post-Archean Australian Shale (PAAS; McLennan, 2001)

For comparison, the REY data of hydrothermal sediments from the Loki's Castle field (Gartman et al., 2024), REE data of bottom sediments from the East Siberian Sea and Laptev Sea (Astakhov et al., 2018) are shown.

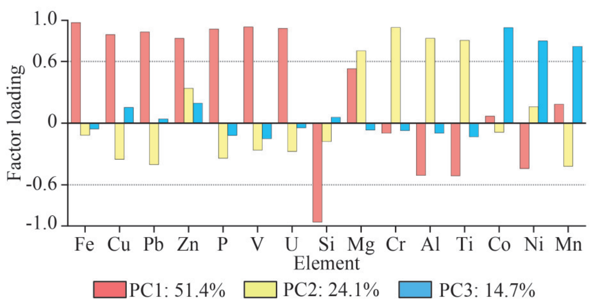

Fig.6 Principal component analysis (PCA) component loadings of PC1, PC2, and PC3 in Core GC02 (0–121 cmbsf)

Cu-Pb-P-V) primarily influences the compositional characteristics of Layers HA1–HA3 (Fig.4), where iron occurs in Fe-(oxyhydr)oxides form (Fig.3a–b, d, g–i). The consistent association of these elements and Fe-(oxyhydr)oxide particles suggests a shared hydrothermal origin, despite weaker enrichment in HA1 and HA3 relative to HA2 (Fig.4). Previous studies have demonstrated that Fe-(oxyhydr)oxides can co-precipitate or scavenge metal elements such as Cu, Zn, and Pb in hydrothermal plume (German et al., 2002; Hrischeva and Scott, 2007; German and Seyfried, 2014). P, V, and U are believed to be scavenged onto hydrothermal Fe-oxyhydroxide particles through seawater-particle interactions (Cave et al., 2002; German and Seyfried, 2014). In contrast to the redox-sensitive metal cluster, the high negative loading of Si of PC1 likely originates from the abundant quartz and aluminosilicate minerals (such as albite and clay) identified in the samples (Fig.3a–b, d, f; Supplementary Fig.S2). Given the limited magmatic activity in the central rift valley where Core GC02 was recovered (Zhang et al., 2024) and the absence of significant volcanic edifices nearby (Fig.2), contributions from in-situ lithic fragments (e.g., basalts) and their alteration products to the sediment composition are likely negligible. Previous studies indicate that the rift valley hosting the study site contains terrigenous sediments hundreds of meters thick (Baker et al., 2004; Rekant and Gusev, 2016; Zhang et al., 2024). Potential transport mechanisms for these terrigenous materials to the study area include sea ice rafting and/or ocean currents (März et al., 2010; Darby et al., 2011). We therefore primarily attributed the PC1 loading of Si to terrigenous inputs. The inverse covariation between these terrigenous components and other elements reflects dilution by hydrothermal plume material. Consequently, the high positive PC1 loadings represent hydrothermal plume fall-out (Fe, Cu, Pb, Zn, P, V, U), while the high negative loadings correspond to terrigenous detritus.

PC2 accounts for 24.1% of the total variance, exhibiting high positive loadings for Al, Ti, Mg, and Cr (Fig.6). Strong correlations (R=0.81–0.96, n=42, P<0.01) exist among Al, Ti, and Cr, consistent with their lithophilic geochemical behavior indicative of terrigenous sources (German et al., 1999; Cave et al., 2002; März et al., 2010). In central Arctic pelagic sediments, Ti and Cr are typically hosted in terrigenous heavy minerals (e.g., anatase), while Al and Mg predominantly reside in aluminosilicates, specifically clay minerals (e.g., illite and chlorite) (Schoster et al., 2000; Martinez et al., 2009; März et al., 2010). Our XRD analyses of GC02 sediments support this association (Supplementary Fig.S2). Therefore, the high positive PC2 loadings primarily represent inputs of pelagic clays and terrigenous rock fragments enriched in Al, Ti, Mg, and Cr.

PC3 accounts for 14.7% of the variance, with positive loadings including Mn, Co, and Ni (Fig.6). This component is interpreted to reflect hydrogenetic Mn oxide precipitation, a process well-documented in Arctic deep-sea sediments (Löwemark et al., 2014; Tessin et al., 2020). Notably, Mn accumulation is particularly enhanced during interglacial periods, likely due to intensified coastal erosion and increased fluvial Mn input from circum-Arctic rivers (Ye et al., 2019; Wiers et al., 2020). The co-occurrence of Co and Ni in this component likely reflects their adsorption onto Mn-oxide surfaces during seawater-column processes (März et al., 2011; Meinhardt et al., 2016). Although Core GC02 is located on a mid-ocean ridge where hydrothermal contributions are possible, the geochemical signatures within Layers M1–M5 exhibit stronger affinities for hydrogenetic processes. Specifically, these layers show subtle positive Ce anomalies (Ce/Ce*= 1.00–1.05; Fig.5), characteristic of seawater-derived Mn oxides precipitated under oscillating redox conditions (Bau et al., 2014; Hein et al., 2017). On this basis, we tentatively interpret PC3 as representing a shelf-derived Mn signal (Mn-Co-Ni) controlled by redox-sensitive sedimentary dynamics on Arctic continental margins (Chiu et al., 2017; Ye et al., 2019).

In summary, three dominant sediment components were identified via PCA in the upper part of Core GC02 (0–121 cmbsf): (1) hydrothermal plume-derived material; (2) terrigenous detritus; and (3) hydrogenetic Mn oxides. Among these, terrigenous component (as indicated by Si and Al) shows consistently high proportions throughout the core (Fig.2), constituting the primary background sediment. The lower core section (121–369 cmbsf) consists of a homogeneous dark greenish-gray clay layer, also primarily composed of terrigenous material (Fig.2; Supplementary Fig.S2). The variance contributions reveal that hydrothermal plume deposition (PC1 positive loadings) is the primary factor controlling sediment geochemical variability, followed by terrigenous inputs (PC1 negative and PC2 positive loadings) and hydrogenetic Mn oxide precipitation (PC3 positive loadings). These relationships illustrate the interplay of complex sediment sources and diverse geological processes in this environment.

5.2 Impact of hydrothermal plume influence on sediment

In Core GC02, PAAS-normalized REY patterns show ratios clustering around unity (Fig.5), indicating the sediments composition predominantly analogous to clay- and silicate-dominated shales. Compared to Loki's Castle sediments, GC02 exhibits elevated REE concentrations (Fig.5), primarily due to its distal location limiting hydrothermal input from REE-depleted sources (Qiu et al., 2023). Although hydrothermal signatures in GC02 may be diluted by terrigenous detritus, they remain discernible through REY systematics (e.g., German et al., 1990; Gartman et al., 2024). To interpret these signatures, we consider the REY fractionation processes during hydrothermal plume evolution. Primary hydrothermal fluids typically exhibit no Ce anomalies (Kuhn et al., 1998; Loges et al., 2012). However, upon mixing with oxygenated seawater, Ce is removed through oxide precipitation, generating hydrothermal plumes containing Fe and Mn oxides characterized by negative Ce anomalies (Ce/Ce*<1) (German et al., 1990; German and Seyfried, 2014; Agarwal et al., 2020). Rapidly precipitated hydrothermal oxides thus typically exhibit negative Ce anomalies due to inhibited cerium accumulation during fast mineral growth (Bau et al., 2014; Gartman et al., 2024). Conversely, hydrogenetic precipitates formed through prolonged seawater interaction develop positive Ce anomalies (Ce/Ce*>1) via continuous REY adsorption (Bau et al., 2014; Hein et al., 2017). Consistent with these processes, Layer HA2 stands out with distinct negative Ce anomalies (Ce/Ce*= 0.82–0.85; Fig.5), being strongly indicative of hydrothermal inputs. This interpretation is further supported by its relative LREE depletion (La_N/Yb_N= 0.84–0.88) and reduced total REE contents (mean ΣREE=182 μg/g; *n*=3), consistent with rapid oxide precipitation processes (Agarwal et al., 2020; Gartman et al., 2024). In contrast, Layer HA3 shows a weaker hydrothermal signal, evidenced by a slight negative Ce anomaly (Ce/Ce*=0.96; Fig.5) and relatively low REE content (ΣREE=185 μg/g; Fig.5). Layer HA1 exhibits elevated total REE concentrations (mean ΣREE=236 μg/g; *n*=2), with one subsample (84–85 cmbsf) showing a distinct positive Ce anomaly (Ce/Ce*=1.05). Given its shared Fe-Cu-Pb-P-V enrichment pattern with the hydrothermal Layer HA2, we infer that Layer HA1 reflects mixed hydrothermal-hydrogenetic inputs (Agarwal et al., 2020), likely resulting from post-depositional interaction of Fe-(oxyhydr)oxides with seawater (Bau and Koschinsky, 2009; Bau et al., 2014).

Europium anomalies (Eu/Eu*) serve as proxies for high-temperature fluid-rock interactions (German and Seyfried, 2014; Yang et al., 2022). However, pelagic background sediments in Core GC02 also exhibit positive Eu anomalies. This characteristic likely arises from source rock inheritance, as REE patterns in sediments from the East Siberian Sea and Laptev Sea (Astakhov et al., 2018) closely mirror those in our samples (Fig.5). Notably, Laptev Sea sediments display elevated total REE concentrations and positive Eu anomalies (mean ΣREE=207 μg/g; mean Eu/Eu*=1.12), aligning with our data and suggesting the Laptev Sea as a primary sediment source. These anomalies probably originate from detritus eroded from the Siberian igneous province (Astakhov et al., 2018). In our study, most layers had consistently positive Eu anomalies (Eu/Eu*=1.11–1.20, mean=1.15; *n*=67), except for HA2 which exhibits significantly higher values (Eu/Eu*=1.23–1.30, mean=1.27; *n*=3). Crucially, HA2 also exhibited pronounced decreases in Si and Al concentrations (Fig.2), key indicators of terrigenous input, which reflect dilution by hydrothermal Fe-(oxyhydr)oxides. This confirms that the Eu anomalies in Layer HA2 are not derived from terrigenous detrital sources. Furthermore, although hydrothermal-affected layers (including HA2) contain coarser-grained and more abundant volcanic glass than other intervals, its abundance remains negligible relative to detrital components like quartz (Fig.3a, c–d). Thus, volcanic glass is unlikely to be a significant source of the observed Eu anomalies. We therefore interpret the pronounced Eu anomalies in HA2 as dominantly originating from hydrothermal Fe-(oxyhydr)oxide inputs, confirming Eu/Eu* remains a reliable hydrothermal indicator in this depositional setting. To further discriminate hydrothermal versus terrigenous contributions, we employed a dual-proxy approach using Eu/Eu* versus Al/(Al+Fe+Mn) (Fig.7). The Al/(Al+Fe+Mn) ratio effectively traces sediment provenance, indicating the relative abundance of detrital aluminosilicates versus hydrothermal components (Boström et al., 1969; Qiu et al., 2023). As shown in Fig.7, HA2 sediments exhibit elevated Eu anomalies coupled with low Al/(Al+Fe+Mn) ratios (Eu/Eu*=1.23–1.30; Al/(Al+Fe+Mn)=0.33–0.41), paralleling proximal hydrothermal sediments (Eu/Eu*=1.13–1.24; Al/(Al+Fe+Mn)=0.25–0.45) from Loki's Castle field (Gartman et al., 2024). This geochemical fingerprint provides additional evidence for strong hydrothermal influence on HA2. Moreover, the predominance of Fe-(oxyhydr)oxides, a diagnostic signature of hydrothermal deposition, further indicates that Layer HA2 incorporates the precipitation of hydrothermal plume particulates (Gartman and Findlay, 2020). Although Layers HA1 and HA3 plot predominantly within the cluster of pelagic background sediments in Fig.7, their minor shifts toward the hydrothermal endmember indicate subtle influence from hydrothermal plume fall-out. Nevertheless, terrigenous components remain volumetrically dominant in these layers.

5.3 Identification and implication of hydrothermal sediment provenance

Marine sediment cores from mid-ocean ridges preserve multiscale geological information, including

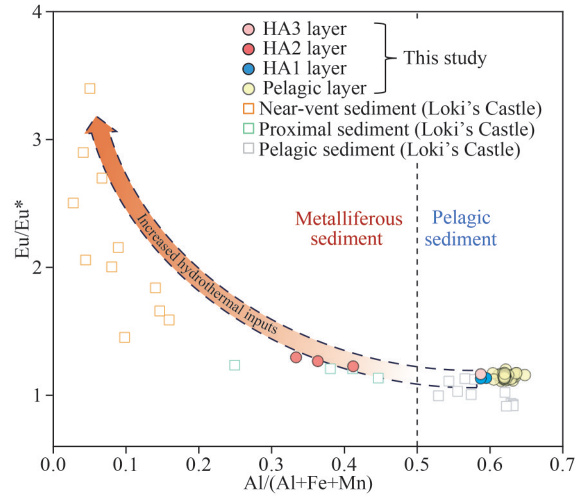

Fig.7 Europium anomaly (Eu/Eu*) vs. Al/(Al+Fe+Mn) ratio of GC02 sediments

Comparative data are sourced from the Loki's Castle hydrothermal field (Gartman et al., 2024) and the Al/(Al+Fe+Mn) ratio of metalliferous sediments is lower than 0.5 (Boström et al., 1969). Hydrothermal sediment from Loki's Castle are classified according to Gartman et al. (2024) as near-vent (mass-wasted oxyhydroxides) and proximal (hydrothermal plume fall-out).

elemental anomalies, volcaniclastic horizons, and hydrothermal metal enrichments, which collectively document magmatic, volcanic, and hydrothermal processes (e.g., German et al., 1999; Gartman et al., 2024). Although the PCA results attributed Mg variations to terrigenous inputs, the hydrothermal Layer HA2 exhibits a pronounced Mg peak alongside significant Si-Al depletions (Fig.2), which are considered as key indicators of terrigenous inputs. This geochemical decoupling is also observed in Layers HA1 and HA3, where Mg remains elevated with coincident Ca and Na peaks (Fig.2). Carbonate dissolution below the CCD and the absence of detrital dolomite preclude biogenic or dolomitic sources for these enrichments. Instead, the correlation between elevated Mg-Ca-Na concentrations and the upward-increasing volcanic glass abundance within HA1–HA3 (Fig.3a, c–d), coupled with compositional matches to Mg-Ca-Na-enriched volcanic glasses documented at the nearby Gakkel Ridge 100°E AVR (Zhang et al., 2024), supports direct volcanic glass provenance for these elements.

The Al-Mg-Fe ternary diagram is used to distinguish hydrothermal precipitates, basaltic debris, ultramafic derivatives, and terrigenous inputs in sediments (Kuhn et al., 2000; Agarwal et al., 2020; Qiu et al., 2023). Hydrothermal sediments of the basalt-hosted vent systems (e.g., the Main Endeavor field, Juan de Fuca Ridge) are typically characterized by Fe-sulfides and Fe-(oxyhydr)oxides, along with detrital low-Mg and high-Al basaltic clasts embedded in a matrix of smectite-zeolite alteration assemblages (Hrischeva and Scott, 2007; Evans et al., 2023). Conversely, under the ultramafic-influenced environment, water-rock reactions between deep-seated hydrothermal fluids and Mg-rich olivine produce talc, and other secondary minerals, resulting in the surrounding sediments being enriched in peridotite fragments, serpentine and talc assemblages (e.g., Dias and Barriga, 2006; Marques et al., 2007; Debret et al., 2018; Albers et al., 2025). In our case (Fig.8), most sediment samples cluster near the Al-rich upper continental crust field, indicating dominant terrigenous provenance without discernible ultramafic contributions. Notably, samples from the hydrothermal-affected layers (HA1–HA3) exhibit a distinct Al-Fe mixing trend. Coupled with the observed enrichment of coarse volcanic glass particles in these layers, we infer that aluminum and magnesium primarily reside in Mg-Al silicates (e.g., clay minerals and albite), with subordinate incorporation in minor mafic volcaniclastic components. Collectively, these results provide evidence that the hydrothermal signatures preserved in the sedimentary core reflect long-range plume dispersion from a vigorous high-temperature hydrothermal system associated with the adjacent high-magma-supply neovolcanic ridge. This interpretation is also supported by a significant hydrothermal plume anomaly (maximum nephelometric turbidity unit (ΔNTU)>0.015; Supplementary Fig.S1) detected along the 100°E AVR during the JASMInE expedition, located approximately 40 km from Core GC02 (Fig.1).

Current investigations have identified only two active hydrothermal fields along the Gakkel Ridge: the Aurora field (Edmonds et al., 2003) located in the western volcanic zone and the Polaris field (Wegener et al., 2024) in the eastern volcanic zone. Both systems exhibit distinct geochemical signatures influenced by ultramafic lithologies derived from deep-seated sources (German et al., 2022; Albers et al., 2025), with their formation and maintenance appearing fundamentally linked to dynamic interactions between melt supply variations and crustal architecture (Coogan and Dosso, 2012). Along the ultra-slow spreading ridges, insufficient melt supply has generated exceptionally thinned crust (1.9–3.3 km in thickness; Jokat et al., 2003). Extensional faulting facilitates hydrothermal fluid circulation through the thin crust, enabling water-rock reactions with underlying ultramafic units (German et al., 2022; Albers et al., 2025). In contrast, the segment of the Gakkel Ridge 92°E–100°E exhibits enhanced melt supply, resulting in the formation of thicker oceanic crust (Tan et al., 2024; Zhang et al., 2024). For example, the crustal thickness of the 100°E AVR (Fig.1) reach up to 8.9 km, while the central rift valley between the 92°E and 100°E AVRs generally exhibits crustal thicknesses exceeding 4 km (Zhang et al., 2024). In similar tectonic settings, the thick crust composed of stacked volcanic and gabbroic sequences may act as a permeability barrier, potentially limiting fluid access to the ultramafic basement rocks (Cannat et al., 2006). Therefore, the significantly thickened oceanic crust within the 92°E–100°E segment makes it feasible to interpret the hydrothermal activity recorded in Core GC02 as originating from a potential basalt-hosted source.

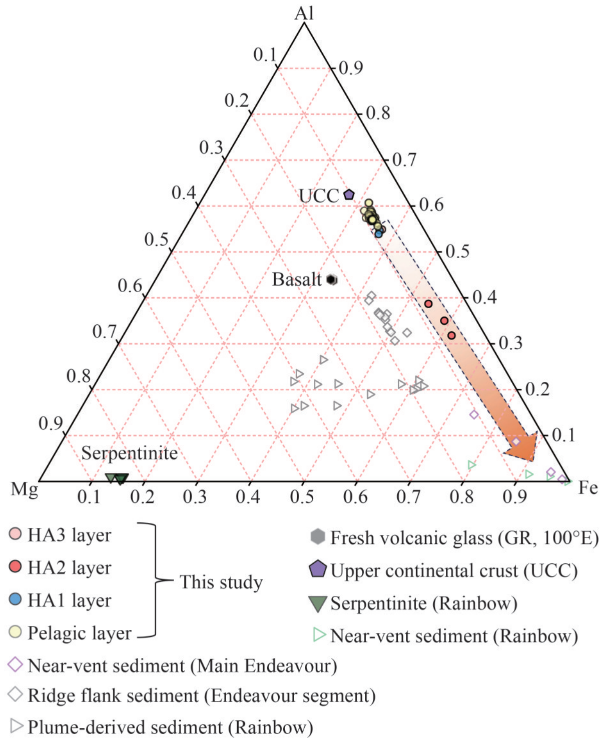

Fig.8 Ternary plot of Al-Fe-Mg for GC02 sediments

The cited data are from the following sources: ridge flank sediments from the Endeavor Segment (Hrischeva and Scott, 2007), hydrothermal sediments from the Main Endeavor field (Hrischeva and Scott, 2007) and the Rainbow fields (Cave et al., 2002; Dias and Barriga, 2006), fresh volcanic glass from the Gakkel Ridge 100°E AVR (Zhang et al., 2024), serpentinites from the Rainbow field (Debret et al., 2018), and upper continental crust (UCC; McLennan, 2001).

6 CONCLUSION

The 369-cm-long sediment Core GC02, recovered from the rift valley of the Gakkel Ridge 96°E, comprises multisource sedimentary components, including terrigenous debris, hydrothermal plume fall-out, volcanic glass, and hydrogenetic Mn oxides. The upper 85-cmbsf interval records three distinct hydrothermal event layers. Among these, Layer HA2 (13–16 cmbsf) exhibits the most diagnostic geochemical signatures in the core, displaying the highest Fe, Mn, Cu, and Pb concentrations, the lowest REE abundances, the most pronounced positive Eu and negative Ce anomalies. Both Layers HA1 (83–85 cmbsf) and HA3 (6–7 cmbsf) contain Fe-(oxyhydr)oxides and exhibit Fe-Cu-Pb-P-V enrichment patterns similar to those of Layer HA2. Although the hydrothermal material abundance and overall elemental enrichment within HA1 and HA3 are significantly lower than in HA2, these layers remain geochemically distinguishable from background pelagic sediments. Collectively, these geochemical patterns collectively indicate pulsating hydrothermal venting and subsequent plume dispersion processes in the study area. Furthermore, systematic covariation of volcanic glass content with hydrothermal signatures, together with diagnostic Al-Fe-Mg ternary signatures, provides compelling evidence that the hydrothermal components were derived from a basalt-hosted hydrothermal system. Our findings not only reveal intense hydrothermal activities recorded in rift sediments distal from the AVR, but also provides new evidence for episodic hydrothermal activities and plume dispersion in the eastern segment of the Gakkel Ridge during geological history.

7 DATA AVAILABILITY STATEMENT

All data generated and analyzed during this study are included in this published article and its supplementary information files.

8 ACKNOWLEDGMENT

The authors thank scientists and crews of Icebreaker *Xuelong* 2 for their support during the on-board survey and sampling. We thank Dr. Jihao ZHU at the SGL for his assistance with the XRF and ICP-MS analyses.

References

Agarwal D K, Roy P, Prakash L S et al. 2020. Hydrothermal signatures in sediments from eastern Southwest Indian Ridge 63°E to 68°E. *Marine Chemistry*, **218**: 103732, https://doi.org/10.1016/j.marchem.2019.103732.

Albers E, Diehl A, Fitzsimmons J N et al. 2025. Ultramafic-influenced submarine venting on basaltic seafloor at the Polaris site, 87°N, Gakkel Ridge. *Earth and Planetary Science Letters*, **651**: 119166, https://doi.org/10.1016/j.epsl.2024.119166.

Astakhov A S, Semiletov I P, Sattarova V V et al. 2018. Rare earth elements in the bottom sediments of the East Arctic seas of Russia as indicators of terrigenous input. *Doklady Earth Sciences*, **482**(2): 1324-1327, https://doi.org/10.1134/S1028334X18100021.

Baker E T, Edmonds H N, Michael P J et al. 2004. Hydrothermal venting in magma deserts: the ultraslow-spreading Gakkel and Southwest Indian Ridges. *Geochemistry*, *Geophysics*, *Geosystems*, **5**(8): Q08002, https://doi.org/10.1029/2004GC000712.

Bau M, Koschinsky A. 2009. Oxidative scavenging of cerium on hydrous Fe oxide: evidence from the distribution of rare earth elements and yttrium between Fe oxides and Mn oxides in hydrogenetic ferromanganese crusts. *Geochemical Journal*, **43**(1): 37-47, https://doi.org/10.2343/geochemj.1.0005.

Bau M, Schmidt K, Koschinsky A et al. 2014. Discriminating between different genetic types of marine ferro-manganese crusts and nodules based on rare earth elements and yttrium. *Chemical Geology*, **381**: 1-9, https://doi.org/10.1016/j.chemgeo.2014.05.004.

Boström K, Peterson M N A, Joensuu O et al. 1969. Aluminum-poor ferromanganoan sediments on active oceanic ridges. *Journal of Geophysical Research*, **74**(12): 3261-3270, https://doi.org/10.1029/JB074i012p03261.

Cannat M, Sauter D, Mendel V et al. 2006. Modes of seafloor generation at a melt-poor ultraslow-spreading ridge. *Geology*, **34**(7): 605-608, https://doi.org/10.1130/G22486.1.

Cave R R, German C R, Thomson J et al. 2002. Fluxes to sediments underlying the Rainbow hydrothermal plume at 36°14′N on the Mid-Atlantic Ridge. *Geochimica et Cosmochimica Acta*, **66**(11): 1905-1923, https://doi.org/10.1016/S0016-7037(02)00823-2.

Chiu P Y, Chao W S, Gyllencreutz R et al. 2017. New constraints on Arctic Ocean Mn stratigraphy from radiocarbon dating on planktonic foraminifera. *Quaternary International*, **447**: 13-26, https://doi.org/10.1016/j.quaint.2016.11.030.

Cochran J R. 2008. Seamount volcanism along the Gakkel Ridge, Arctic Ocean. *Geophysical Journal International*, **174**(3): 1153-1173, https://doi.org/10.1111/j.1365-246X.2008.03860.x.

Coogan L A, Attar A, Mihaly S F et al. 2017. Near-vent chemical processes in a hydrothermal plume: insights from an integrated study of the Endeavour segment. *Geochemistry*, *Geophysics*, *Geosystems*, **18**(4): 1641-1660, https://doi.org/10.1002/2016GC006747.

Coogan L A, Dosso S. 2012. An internally consistent, probabilistic, determination of ridge-axis hydrothermal fluxes from basalt-hosted systems. *Earth and Planetary Science Letters*, **323-324**: 92-101, https://doi.org/10.1016/j.epsl.2012.01.017.

Darby D A, Myers W B, Jakobsson M et al. 2011. Modern dirty sea ice characteristics and sources: the role of anchor ice. *Journal of Geophysical Research*, **116**(C9):

C09008, https://doi.org/10.1029/2010JC006675.

Debret B, Beunon H, Mattielli N et al. 2018. Ore component mobility, transport and mineralization at mid-oceanic ridges: a stable isotopes (Zn, Cu and Fe) study of the Rainbow massif (Mid-Atlantic Ridge 36°14′N). *Earth and Planetary Science Letters*, **503**: 170-180, https://doi.org/10.1016/j.epsl.2018.09.009.

Dias Á S, Barriga F J A S. 2006. Mineralogy and geochemistry of hydrothermal sediments from the serpentinite-hosted Saldanha hydrothermal field (36°34′N; 33°26′W) at MAR. *Marine Geology*, **225**(1-4): 157-175, https://doi.org/10.1016/j.margeo.2005.07.013.

Ding W W, Niu X W, Zhang T et al. 2022. Submarine wide-angle seismic experiments in the High Arctic: the JASMInE Expedition in the slowest spreading Gakkel Ridge. *Geosystems and Geoenvironment*, **1**(3): 100076, https://doi.org/10.1016/j.geogeo.2022.100076.

Edmonds H N, Michael P J, Baker E T et al. 2003. Discovery of abundant hydrothermal venting on the ultraslow-spreading Gakkel ridge in the Arctic Ocean. *Nature*, **421**(6920): 252-256, https://doi.org/10.1038/nature01351.

Egozcue J J, Pawlowsky-Glahn V, Mateu-Figueras G et al. 2003. Isometric Logratio transformations for compositional data analysis. *Mathematical Geology*, **35**(3): 279-300, https://doi.org/10.1023/A:1023818214614.

Evans G N, Coogan L A, Kaçar B et al. 2023. Molybdenum in basalt-hosted seafloor hydrothermal systems: experimental, theoretical, and field sampling approaches. *Geochimica et Cosmochimica Acta*, **353**: 28-44, https://doi.org/10.1016/j.gca.2023.05.018.

Früh-Green G L, Kelley D S, Lilley M D et al. 2022. Diversity of magmatism, hydrothermal processes and microbial interactions at mid-ocean ridges. *Nature Reviews Earth & Environment*, **3**(12): 852-871, https://doi.org/10.1038/s43017-022-00364-y.

Gartman A, Findlay A J. 2020. Impacts of hydrothermal plume processes on oceanic metal cycles and transport. *Nature Geoscience*, **13**(6): 396-402, https://doi.org/10.1038/s41561-020-0579-0.

Gartman A, Payan D, Au M et al. 2024. Hydrothermal plume fallout, mass wasting, and volcanic eruptions contribute to sediments at Loki's Castle vent field, Mohns Ridge. *Geochemistry*, *Geophysics*, *Geosystems*, **25**(2): e2023GC011094, https://doi.org/10.1029/2023GC011094.

German C R, Colley S, Palmer M R et al. 2002. Hydrothermal plume-particle fluxes at 13°N on the East Pacific Rise. *Deep Sea Research Part I*: *Oceanographic Research Papers*, **49**(11): 1921-1940, https://doi.org/10.1016/S0967-0637(02)00086-9.

German C R, Hergt J, Palmer M R et al. 1999. Geochemistry of a hydrothermal sediment core from the OBS vent-field, 21°N East Pacific Rise. *Chemical Geology*, **155**(1-2): 65-75, https://doi.org/10.1016/S0009-2541(98)00141-7.

German C R, Klinkhammer G P, Edmond J M et al. 1990. Hydrothermal scavenging of rare-earth elements in the ocean. *Nature*, **345**(6275): 516-518, https://doi.org/10.1038/345516a0.

German C R, Petersen S, Hannington M D. 2016. Hydrothermal exploration of mid-ocean ridges: where might the largest sulfide deposits be forming? *Chemical Geology*, **420**: 114-126, https://doi.org/10.1016/j.chemgeo.2015.11.006.

German C R, Reeves E P, Türke A et al. 2022. Volcanically hosted venting with indications of ultramafic influence at Aurora hydrothermal field on Gakkel Ridge. *Nature Communications*, **13**(1): 6517, https://doi.org/10.1038/s41467-022-34014-0.

German C R, Seyfried W E Jr. 2014. Hydrothermal processes. *Treatise on Geochemistry* (*Second Edition*), **8**: 191-233, https://doi.org/10.1016/B978-0-08-095975-7.00607-0.

Hein J R, Konstantinova N, Mikesell M et al. 2017. Arctic deep water ferromanganese-oxide deposits reflect the unique characteristics of the Arctic Ocean. *Geochemistry*, *Geophysics*, *Geosystems*, **18**(11): 3771-3800, https://doi.org/10.1002/2017GC007186.

Hrischeva E, Scott S D. 2007. Geochemistry and morphology of metalliferous sediments and oxyhydroxides from the Endeavour segment, Juan de Fuca Ridge. *Geochimica et Cosmochimica Acta*, **71**(14): 3476-3497, https://doi.org/10.1016/j.gca.2007.03.024.

Jokat W, Ritzmann O, Schmidt-Aursch M C et al. 2003. Geophysical evidence for reduced melt production on the Arctic ultraslow Gakkel mid-ocean ridge. *Nature*, **423**(6943): 962-965, https://doi.org/10.1038/nature01706.

Jutterström S, Anderson L G. 2005. The saturation of calcite and aragonite in the Arctic Ocean. *Marine Chemistry*, **94**: 101-110, https://doi.org/10.1016/j.marchem.2004.08.010.

Kuhn T, Bau M, Blum N et al. 1998. Origin of negative Ce anomalies in mixed hydrothermal-hydrogenetic Fe-Mn crusts from the Central Indian Ridge. *Earth and Planetary Science Letters*, **163**(1-4): 207-220, https://doi.org/10.1016/S0012-821X(98)00188-5.

Kuhn T, Burger H, Castradori D et al. 2000. Volcanic and hydrothermal history of ridge segments near the Rodrigues Triple Junction (Central Indian Ocean) deduced from sediment geochemistry. *Marine Geology*, **169**(3-4): 391-409, https://doi.org/10.1016/S0025-3227(00)00080-3.

Liao S L, Tao C H, Li H M et al. 2018. Surface sediment geochemistry and hydrothermal activity indicators in the Dragon Horn area on the Southwest Indian Ridge. *Marine Geology*, **398**: 22-34, https://doi.org/10.1016/j.margeo.2017.12.005.

Loges A, Wagner T, Barth M et al. 2012. Negative Ce anomalies in Mn oxides: the role of Ce^{4+} mobility during water-mineral interaction. *Geochimica et Cosmochimica Acta*, **86**: 296-317, https://doi.org/10.1016/j.gca.2012.03.017.

Löwemark L, März C, O'Regan M et al. 2014. Arctic Ocean Mn-stratigraphy: genesis, synthesis and inter-basin correlation. *Quaternary Science Reviews*, **92**: 97-111, https://doi.org/10.1016/j.quascirev.2013.11.018.

Marques A F A, Barriga F J A S, Scott S D. 2007. Sulfide mineralization in an ultramafic-rock hosted seafloor hydrothermal system: from serpentinization to the formation of Cu-Zn-(Co)-rich massive sulfides. *Marine Geology*, **245**(1-4): 20-39, https://doi.org/10.1016/j.margeo.2007.05.007.

Martinez N C, Murray R W, Dickens G R et al. 2009.

Discrimination of sources of terrigenous sediment deposited in the central Arctic Ocean through the Cenozoic. *Paleoceanography*, **24**(1): PA1210, https://doi.org/10.1029/2007PA001567.

März C, Schnetger B, Brumsack H J. 2010. Paleoenvironmental implications of Cenozoic sediments from the central Arctic Ocean (IODP Expedition 302) using inorganic geochemistry. *Paleoceanography*, **25**(3): PA3206, https://doi.org/10.1029/2009PA001860.

März C, Stratmann A, Matthiessen J et al. 2011. Manganese-rich brown layers in Arctic Ocean sediments: composition, formation mechanisms, and diagenetic overprint. *Geochimica et Cosmochimica Acta*, **75**(23): 7668-7687, https://doi.org/10.1016/j.gca.2011.09.046.

McLennan S M. 2001. Relationships between the trace element composition of sedimentary rocks and upper continental crust. *Geochemistry*, *Geophysics*, *Geosystems*, **2**(4): 2000GC000109, https://doi.org/10.1029/2000GC000109.

Meinhardt A K, März C, Schuth S et al. 2016. Diagenetic regimes in Arctic Ocean sediments: implications for sediment geochemistry and core correlation. *Geochimica et Cosmochimica Acta*, **188**: 125-146, https://doi.org/10.1016/j.gca.2016.05.032.

Michael P J, Langmuir C H, Dick H J B et al. 2003. Magmatic and amagmatic seafloor generation at the ultraslow-spreading Gakkel ridge, Arctic Ocean. *Nature*, **423**(6943): 956-961, https://doi.org/10.1038/nature01704.

Mills R, Elderfield H, Thomson J. 1993. A dual origin for the hydrothermal component in a metalliferous sediment core from the Mid-Atlantic Ridge. *Journal of Geophysical Research*: *Solid Earth*, **98**(B6): 9671-9681, https://doi.org/10.1029/92JB01414.

O'Connor J M, Jokat W, Michael P J et al. 2021. Thermochemical anomalies in the upper mantle control Gakkel Ridge accretion. *Nature Communications*, **12**(1): 6962, https://doi.org/10.1038/s41467-021-27058-1.

Pelleter E L, Principaud M, Alix A S et al. 2024. Diversity, spatial distribution and evolution of inactive and weakly active hydrothermal deposits in the TAG hydrothermal field. *Frontiers in Earth Science*, **12**: 1304993, https://doi.org/10.3389/feart.2024.1304993.

Qiu Z Y, Han X Q, Fan W J et al. 2023. Hydrothermal signatures and prospecting indicators in sediments along the Carlsberg Ridge. *Sedimentary Geology*, **458**: 106536, https://doi.org/10.1016/j.sedgeo.2023.106536.

Rekant P V, Gusev E A. 2016. Sediments in the Gakkel Ridge rift zone (*Arctic ocean*): structure and history. *Russian Geology and Geophysics*, **57**(9): 1283-1287, https://doi.org/10.1016/j.rgg.2016.08.013.

Rusakov V Y, Levitan M A, Roshchina I A et al. 2010. Chemical composition of late Pleistocene-Holocene pelagic sediments in Gakkel Ridge, Arctic Ocean. *Geochemistry International*, **48**(10): 999-1013, https://doi.org/10.1134/S0016702910100058.

Schoster F, Behrends M, Müller C et al. 2000. Modern river discharge and pathways of supplied material in the Eurasian Arctic Ocean: evidence from mineral assemblages and major and minor element distribution. *International Journal of Earth Sciences*, **89**(3): 486-495, https://doi.org/10.1007/s005310000120.

Stranne C, Sohn R A, Liljebladh B et al. 2010. Analysis and modeling of hydrothermal plume data acquired from the 85°E segment of the Gakkel Ridge. *Journal of Geophysical Research*: *Oceans*, **115**(C6): C06028, https://doi.org/10.1029/2009JC005776.

Tan P C, Breivik A J, Ding W W et al. 2024. Unexpectedly high magma productivity inferred from crustal roughness and residual bathymetry on the eastern part of the ultra-slow spreading Gakkel Ridge since ~45 Ma, Eurasian Basin, Arctic Ocean. *Journal of Geophysical Research*: *Solid Earth*, **129**(6): e2023JB028470, https://doi.org/10.1029/2023JB028470.

Tessin A, März C, Blais M A et al. 2020. Arctic continental margin sediments as possible Fe and Mn sources to seawater as sea ice retreats: insights from the Eurasian margin. *Global Biogeochemical Cycles*, **34**(8): e2020GB006581, https://doi.org/10.1029/2020GB006581.

Wang W Z, Huang X, Chen S et al. 2024. Geochemical characteristics of sediments in the southern Mid-Atlantic Ridge indicate hydrothermal activity: evidence from rare earth elements. *Marine and Petroleum Geology*, **168**: 107041, https://doi.org/10.1016/j.marpetgeo.2024.107041.

Wegener G, Molari M, Purser A et al. 2024. Hydrothermal vents supporting persistent plumes and microbial chemoautotrophy at Gakkel Ridge (Arctic Ocean). *Frontiers in Microbiology*, **15**: 1473822, https://doi.org/10.3389/fmicb.2024.1473822.

Wiers S, Snowball I, O'Regan M et al. 2020. The Arctic Ocean manganese cycle, an overlooked mechanism in the anomalous palaeomagnetic sedimentary record. *Frontiers in Earth Science*, **8**: 75, https://doi.org/10.3389/feart.2020.00075.

Yang B J, Liu J H, Li C S et al. 2022. Mineralogical and geochemical characteristics of near-vent metalliferous sediments: implications for hydrothermal processes along the southern Mid-Atlantic ridge (12°S-28°S). *Ore Geology Reviews*, **148**: 105003, https://doi.org/10.1016/j.oregeorev.2022.105003.

Ye L M, März C, Polyak L et al. 2019. Dynamics of manganese and cerium enrichments in Arctic Ocean sediments: a case study from the Alpha Ridge. *Frontiers in Earth Science*, **6**: 236, https://doi.org/10.3389/feart.2018.00236.

Zhang T, Li J B, Niu X W et al. 2024. Highly variable magmatic accretion at the ultraslow-spreading Gakkel Ridge. *Nature*, **633**(8028): 109-113, https://doi.org/10.1038/s41586-024-07831-0.

Electronic supplementary material

Supplementary material (Supplementary Figs. S1–S2 and Supplementary Tables S1–S2) is available in the online version of this article at https://doi.org/10.1007/s00343-025-5112-2.